



EAST-Educational Adaptive-optics Solar Telescope

Changhui Rao^{1,2,3}, Xuejun Rao^{1,2}, Zhimao Du⁴, Hua Bao^{1,2}, Cheng Li^{1,2}, Jinlong Huang¹, Youming Guo^{1,2}, Libo Zhong^{1,2}, Qing Lin⁴, Xin Ge⁴, Jinsheng Yang^{1,2}, Xinlong Fan^{1,2}, Yangyi Liu⁵, Dan Jia¹, Xin Li¹, Mei Li^{1,2}, Ming Zhang¹, Yuntao Cheng¹, Jiahui Zhou^{1,2,3}, Jiawen Yao⁴, Lanqiang Zhang^{1,2}, and Naiting Gu^{1,2}

¹The Institute of Optics and Electronics, Chinese Academy of Sciences, Chengdu 610209, China; chrhao@ioe.ac.cn

²The Key Laboratory on Adaptive Optics, Chinese Academy of Sciences, Chengdu 610209, China

³The University of Chinese Academy of Sciences, Beijing 10049, China

⁴Shanghai Astronomy Museum, Shanghai 201306, China

⁵Sichuan Police College, Luzhou 646000, China

Received 2022 January 26; revised 2022 April 2; accepted 2022 April 5; published 2022 May 20

Abstract

For the public having a better understanding of solar activities, the Educational Adaptive-optics Solar Telescope (EAST) was built in July 2021 and is located at the Shanghai Astronomy Museum. The EAST consists of a 65 cm aperture solar telescope with a 177-element adaptive optics system and two-channel high resolution imaging system at the $H\alpha$ and TiO bands, in addition to three full disk solar telescopes at Ca K, $H\alpha$ and TiO bands equipped on the tube of the main telescope. In this paper, the configuration of the EAST is described. Its performance and on-sky observational results are presented. The EAST, to our knowledge, is the most advanced solar telescope for the popularization of science in the world. Due to its excellent performance, the data acquired by the EAST can also be used for research on solar physics and space weather prediction.

Key words: instrumentation: adaptive optics – instrumentation: high angular resolution – techniques: high angular resolution – Sun: general

1. Introduction

With the development of the economy, solar activity has become closely related to human life. In order to study solar activity, various types of solar observation equipments have been developed. Large-aperture solar telescopes play important roles in solar observation and research. In recent years, solar high-resolution observation instruments were rapidly developed, such as the 1 m New Vacuum Solar Telescope (Liu et al. 2014), the 1.5 m GREGOR Solar Telescope, the 1.6 m Goode Solar Telescope (Cao et al. 2010), the 1.8 m Chinese Large Solar Telescope (CLST) (Rao et al. 2015, 2020), the 4 m Daniel K. Inouye Solar Telescope (DKIST) (Rimmele et al. 2020) and the developing 2.5 m WeHoT Solar Telescope (Fang et al. 2019) and 4 m European Solar Telescope (Collados et al. 2013). Those instruments enable people to understand the fine structure of the Sun, not just large-scale activities.

The construction of solar telescopes for public outreach in planetariums or museums can be traced back to the 1920s (Kisskinova et al. 2011). Solar telescopes in museums with an aperture larger than 30 cm can be roughly divided into two categories according to the optical system. The first category uses the celestial optical system, and usually has a tower-shaped architecture with large size. All early solar telescopes are constructed like such a system. The solar tower of the Deutsches Museum was built in 1925. Sunlight is directed through the celestial optical system for splitting. One of the

beams can form a 1 m diameter white light image, and the other can form a solar spectrum through the reflective grating. The Griffith Solar Tower was built in 1935 (Leslie & Margolis 2017). Its celestial optical system uses a set of three plane mirrors to reflect sunlight into three different directions, realizing solar white light image projection, direct human eye observation and diffraction grating spectral observation.

The other category is solar telescopes using the Gregorian optical system which were implemented in later solar systems. The Beijing Planetarium Solar Vacuum Telescope was built in 2004. It consists of a 30 cm diameter primary mirror and four 8 cm diameter telescopes. It can project a 1.8 m white light solar image. The Solar Vacuum Telescope of the Nagoya City Science Museum in Japan was built in 2010. It has a diameter of 30 cm and can form a white light image with a diameter of 1.9 m. The solar tower of Hong Kong's Ma Wan Park was completed in July 2012. The web site of the tower is <http://www.mawanpark.com/eng/attractions/solar-tower.html>. It has a 35 cm diameter vacuum solar telescope, which can form a white light image with a diameter of 1 m.

To give the public a more intuitive understanding of the phenomena and laws of solar activity, like other planetariums, the Shanghai Astronomy Museum (Shanghai Science and Technology Museum Branch) proposed the idea of building a solar tower. In addition to observing the Sun, a visitor can also see how the solar telescope works. After one year of



Figure 1. The 65 cm solar telescope and optical table with the adaptive optics system and two-channel high resolution imaging systems in the Coudé room.

monitoring the daytime visibility in the Lingang area, it was found that the average daytime seeing in the Lingang area was $r_0 \geq 3$ cm. We experimentally applied adaptive optics (AO) technology (Rao et al. 2003, 2010, 2016b) to the solar telescope to make up for the lack of seeing condition in this site.

The Educational Adaptive-optics Solar Telescope (EAST) is designed to simultaneously obtain high-resolution images of the active region and full disk images of the solar photosphere and chromosphere. The full disk solar telescope is integrated into the main telescope instead of building separately. To achieve better results under strong turbulence conditions, an advanced solar AO system (Kong et al. 2016; Rao et al. 2016a, 2018) is equipped on the telescope.

In this paper, we will introduce the solar telescope, including the optical configuration, mechanical system and thermal control system in Section 2. In Section 3, the solar AO system is described and the system performances are evaluated. In Section 4, the imaging system and on-sky observational results of the EAST are reported. Finally, we conclude the work.

2. System Configuration

EAST, shown in Figure 1, is composed of a 65 cm aperture solar telescope with a 177-element adaptive optics system and two-channel high resolution imaging systems at the $H\alpha$ (656.28 nm) and TiO (705.8 nm) bands. Moreover, three full disk solar telescopes at Ca K (393.4 nm), $H\alpha$ and TiO bands are mounted on the tube of the main telescope for solar observation.

EAST employs a two-mirror Gregorian configuration. The spectral range of the telescope is from 0.4 to 1.6 μm . The complete optical design of EAST is drawn in Figure 2. The focal length of the primary mirror M1 is 900 mm, corresponding to the focal ratio of about $f/1.43$. M1 uses ULE®

(Ultra-Low Expansion Glass) material. The surface-shape rms error is about $\lambda/40$ ($\lambda = 632.8$ nm). At the prime focus (F1), there is a field stop (heat stop). The elliptical secondary mirror M2 provides the Coudé focus F2. The main optical parameters of the telescope system are listed in Table 1.

For the vacuum tube of EAST, the experimental results for the heat stop during about 8 hr are plotted in Figure 3. It can be seen that the temperature difference between the heat stop and the outside condition is controlled within $\pm 1^\circ\text{C}$ (Liu et al. 2015).

The tracking performance of EAST is displayed in Figures 4 and 5. The low velocity solar tracking rms errors during 80 s are 0.12'' and 0.11'' for azimuth and elevation axis, respectively. The corresponding long time solar tracking root mean square (rms) errors during 800 s are 0.''19 and 0.''28. The high-performance servo control system provides continuous and stable tracking for the telescope, reduces the workload of the AO system, and ensures clarity and stability of the images.

In the EAST, both full disk solar imaging and high resolution imaging systems are installed. The high-resolution images are obtained after AO correction to improve the quality of the observations. The details of the AO system and the imaging system are described below.

3. Solar AO System

The optical design of the solar AO system is illustrated in Figure 6. The light from the telescope transmits to the AO system and then is collimated by the lens collimator. The AO system is composed of a tip/tilt mirror (TM), a deformable mirror (DM), a correlation Shack-Hartmann wavefront sensor (WFS) and a high speed real time controller (RTC). An zoomed view of the optical system is also depicted in Figure 6, and it is used to convert the diameter between DM and WFS. After AO,

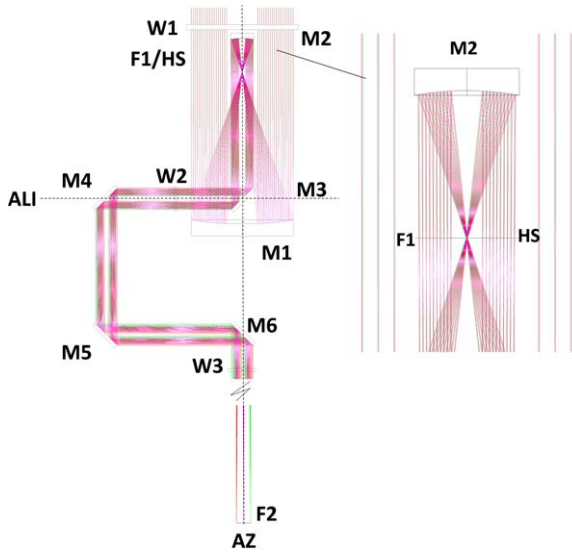


Figure 2. Optical configuration of the EAST (main optical system).

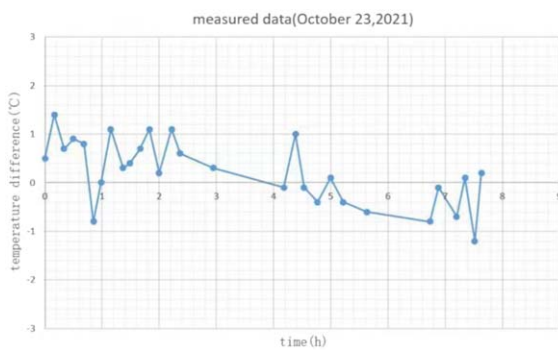


Figure 3. The temperature control results for the heat stop.

Table 1
The Optical Parameters of the Telescope System

| No | Parameter | Value |
|----|-----------------------|-----------------------|
| 1 | Aperture size of M1 | 630 mm |
| 2 | FoV | $\sim 6'$ |
| 3 | Wavelength coverage | 400 nm \sim 1600 nm |
| 4 | Image space f ratio | $f/118$ |
| 5 | Focal Length | ~ 74 m |

two-channel high resolution imaging systems at the $H\alpha$ and TiO bands respectively are installed.

The arrangement of sub-apertures of WFS and the corresponding actuators of DM is shown in Figure 7. The number of DM actuators is 177. The main parameters of the WFS and DM

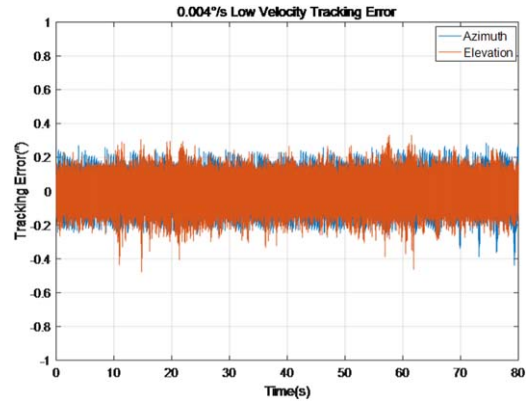


Figure 4. 0.004 s^{-1} low velocity solar tracking error (rms $0''.12$ and $0''.11$).

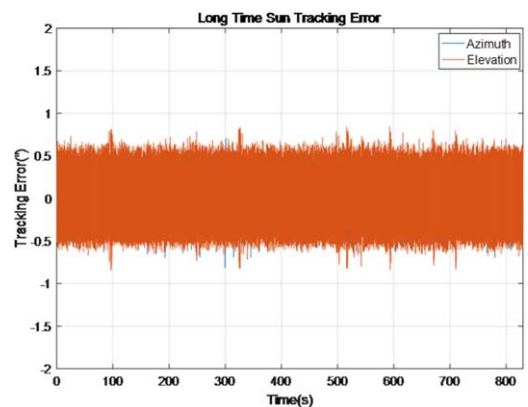


Figure 5. Long time solar tracking error (rms $0''.19$ and $0''.28$)

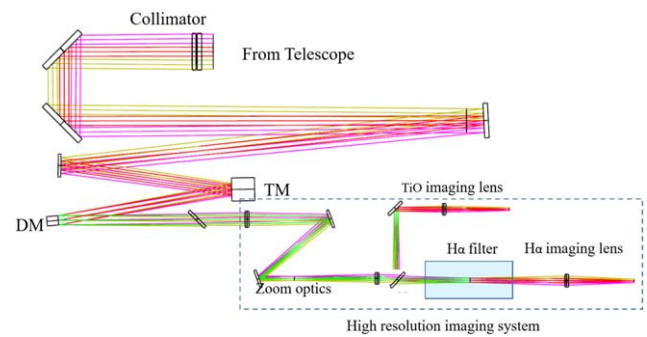


Figure 6. Optical structure of AO system for the EAST.

are listed in Table 2. The correction ability of this configuration for the first 65 modes of the Zernike aberrations (Noll 1976) is displayed in Figure 8.

The WFS detector implemented in the AO system is an EoSens 3CL CMOS Camera, which delivers 8 bit-per pixel

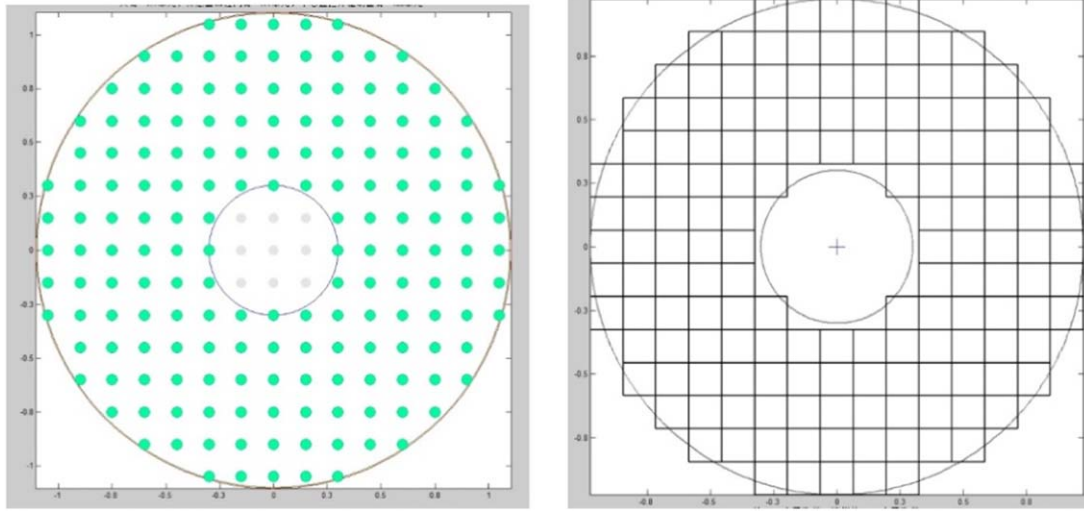


Figure 7. The correspondence between the actuators of DM and the subapertures of WFS.

Table 2
The Parameters of the WFS and DM

| Instrument | Parameter | Value |
|------------|---------------------------|--|
| WFS | Geometry of subapertures | Square |
| | FOV per subaperture | $24'' \times 24''$ |
| | Frame rate of camera | 4000 Hz |
| | Pixel scale | $1''.0 \text{ pixel}^{-1}$ |
| | Clear aperture of DM | 39 mm |
| DM | Number of actuators of DM | 177 |
| | Stroke | $\pm 2.6 \mu\text{m}$ |
| | Original fitting error | $0.11\lambda \text{ PV}$ and $0.011\lambda \text{ rms}$ ($\lambda = 632.8 \text{ nm}$). |

data in the region of 360×360 pixels, at the frame rate of 4000 Hz. The WFS subaperture is arranged as 15×15 and the number of effective subapertures is 140, therefore the number of pixels per subaperture and the reference image size are both 24×24 pixels.

In the EAST AO system, the calculation of cross-correlation between live image $I_L(N \times N \text{ pixels})$ and reference image $I_R(N \times N \text{ pixels})$ by fast Fourier transform (FFT) takes the form as follows

$$C(x, y) = F^{-1}[R^*(u, v)L(u, v)] \quad (1)$$

where $R(u, v)$ and $L(u, v)$ are the Fourier transform of $I_R(x, y)$ and $I_L(x, y)$ respectively, “*” represents complex conjugate, “ F^{-1} ” represents the inverse Fourier transform, and $C(x, y)$ is the cross-correlation results in the spatial domain.

Before the Fourier transform, the reference image needs to be multiplied by a Hamming window to eliminate the influence of truncated sampling on the spectrum. The Hamming window

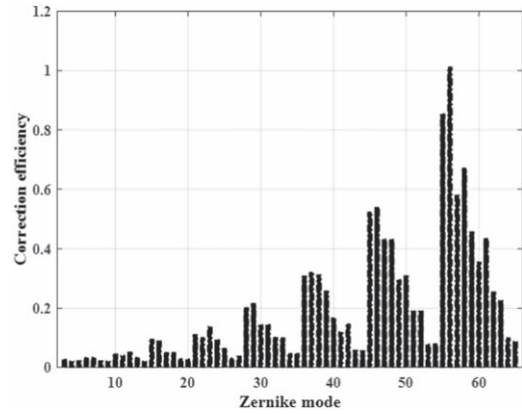


Figure 8. The correction ability for the first 65 modes of the Zernike aberrations.

takes the form as follows

$$W(x, y) = \left[(1 - \alpha) - \alpha * \cos \frac{2\pi x}{N-1} \right] * \left[(1 - \alpha) - \alpha * \cos \frac{2\pi y}{N-1} \right], \quad (2)$$

where α is usually taken as 0.46.

The RTC is employed to extract the gradient of each subaperture, meanwhile the RTC uses the average gradient of all the subapertures to control the fine tracking loop and relies on the reconstructed wavefront information to control the high order correction loop simultaneously.

To meet the demand of timing delay and jitter, the RTC platform is a custom-built architecture based on two advanced Xilinx-series FPGA cards, one for data acquisition and another

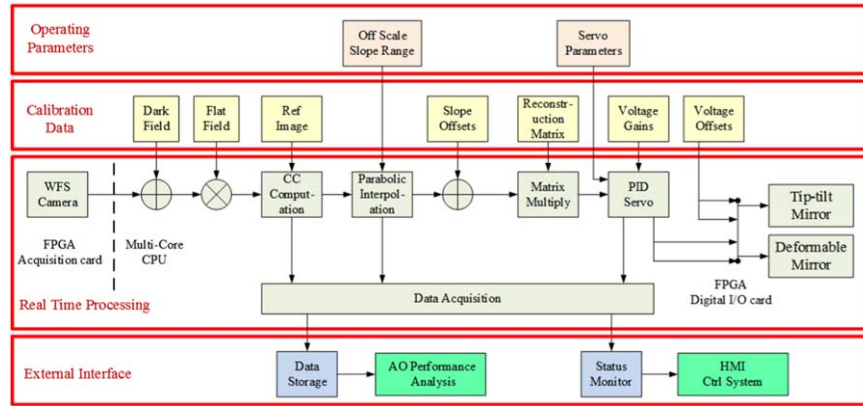


Figure 9. Real time processing of RTC.

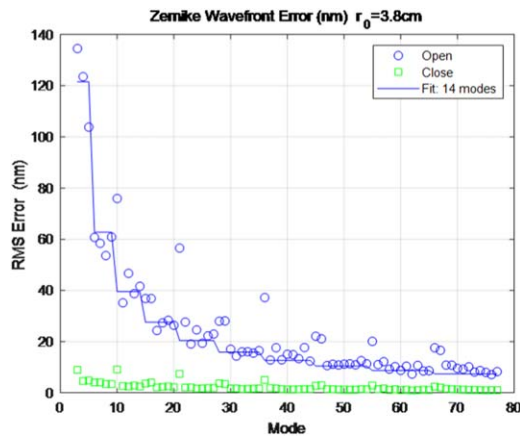


Figure 10. Comparison of the Zernike rms error in open loop (circle) and closed loop (square) modes. The solid curve is the fitting of the Kolmogorov turbulence model to the open loop data.

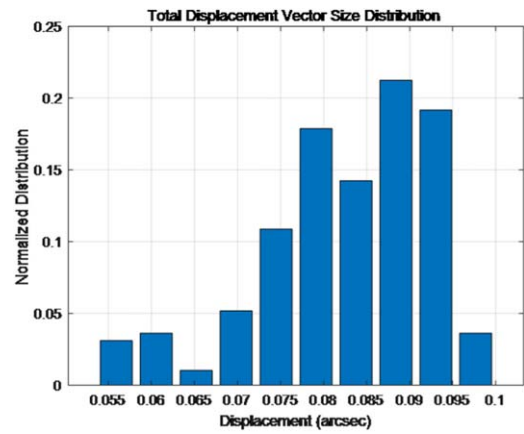


Figure 12. Closed-loop image shift vector length distribution at the time (UT) between 2:47 and 3:03 on 2021 October 3.

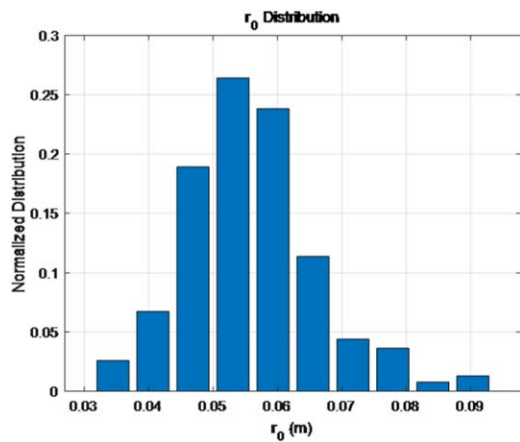


Figure 11. The distribution of r_0 at the time (UT) between 2:47 and 3:03 on 2021 October 3.

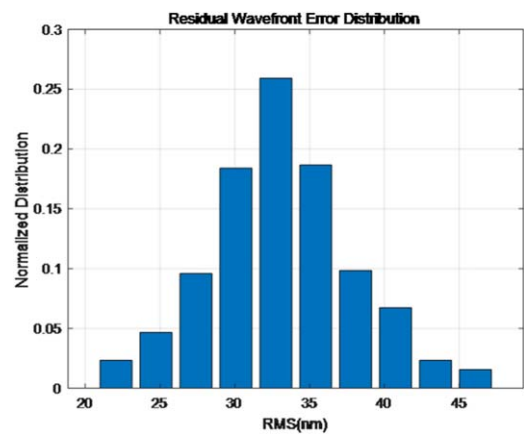


Figure 13. Residual wavefront error distribution at the time (UT) between 2:47 and 3:03 on 2021 October 3.

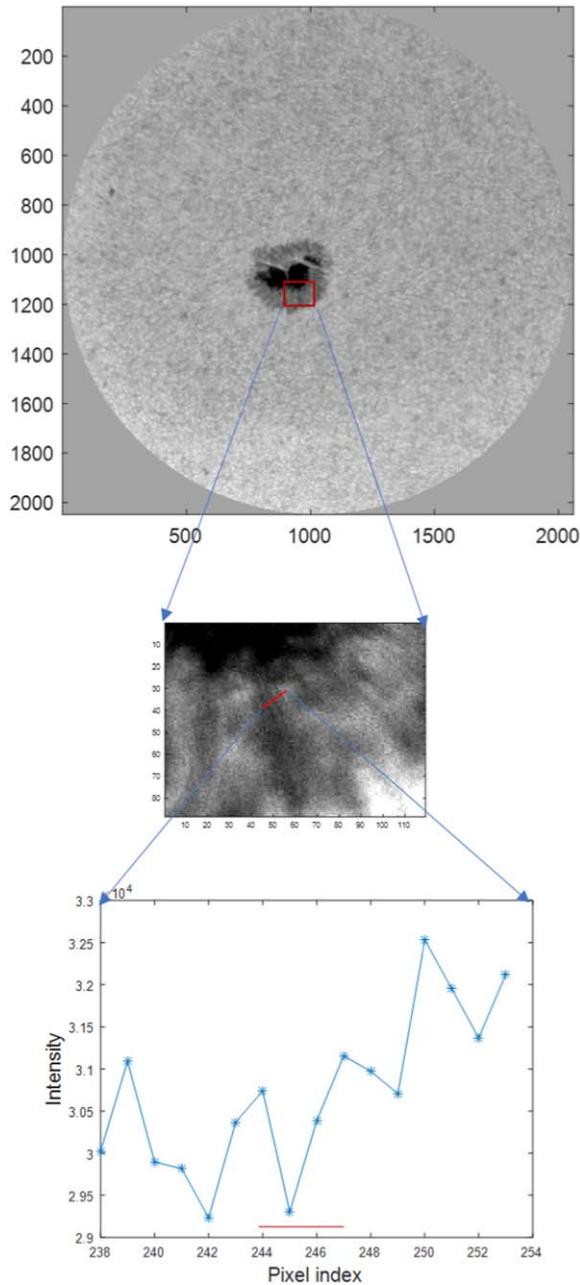


Figure 14. An unsharp masked and intensity-clipped image of solar penumbra fibers.

for digital data I/O, and a $\times 86$ Multi-core CPU computing server with Linux CentOS 8.2 operating system. The real time processing is depicted in Figure 9, in which WFS camera images are acquired by a field-programmable gate array (FPGA) acquisition card, the control signals of TM and DM are transformed by FPGA digital I/O card, and dark field and flat field preprocessing, cross-correlation computation, parabolic interpolation, wavefront reconstruction and proportional-integral-differential (PID) servo are accomplished in a multi-core CPU.

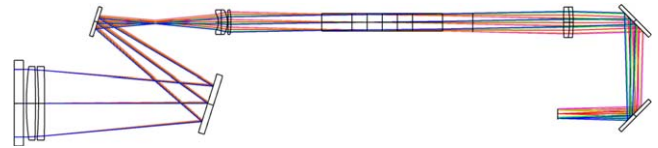


Figure 15. The layout of the full solar imaging system targeting the chromosphere ($H\alpha$ band) for the EAST.

Table 3
The Parameters of the Imaging Optical System

| Imaging system | Parameter | Value |
|-----------------------------------|------------------|------------|
| Full disk Ca K imaging | Wavelength | 393.37 nm |
| | Bandwidth | 0.08 nm |
| | FoV | 42' |
| | Pixel resolution | 0''64 |
| Full disk $H\alpha$ imaging | Wavelength | 656.281 nm |
| | Bandwidth | 0.05 nm |
| | FoV | 37' |
| Full disk TiO imaging | Pixel resolution | 0''56 |
| | Wavelength | 705.74 nm |
| | Bandwidth | 0.5 nm |
| | FoV | 66' |
| High resolution $H\alpha$ imaging | Pixel scale | 1''04 |
| | Wavelength | 656.281 nm |
| | Bandwidth | 0.025 nm |
| | FoV | 4'2 |
| High resolution TiO imaging | Pixel resolution | 0''12 |
| | Wavelength | 705.72 nm |
| | Bandwidth | 0.5 nm |
| | FoV | 4'2 |
| | Pixel resolution | 0''12 |

In implementation, the kernel of the Linux operating system is modified to a real and non-real time dual-kernel mechanism for different computing tasks. The CPU instruction sets and 512 bit, 256 bit and 128 bit registers are effectively utilized to optimize computation, so all the four arithmetic operations of up to 16 bit float can be calculated simultaneously in one CPU instruction cycle. By this way and integrated with the multi-core parallel method, RTC computing resources are fully released. Finally, combined with the classical parallel acceleration techniques, such as pipeline, systolic array and multi-channels/cores parallelism, the total timing delay of about $160 \mu\text{s}$ and jitter of about $\pm 20.0 \mu\text{s}$ are achieved to make the system be the fastest solar AO system until now.

The performance of the AO system is evaluated. The WFS measurements and the DM commands recorded by the RTC are first used to calculate the pseudo open loop wavefront in order to estimate the seeing. Then, the performance including tracking and high-order loop correction is evaluated.

The seeing during observation is estimated by fitting the variances of open loop Zernike modes, from the 3rd to 14th,

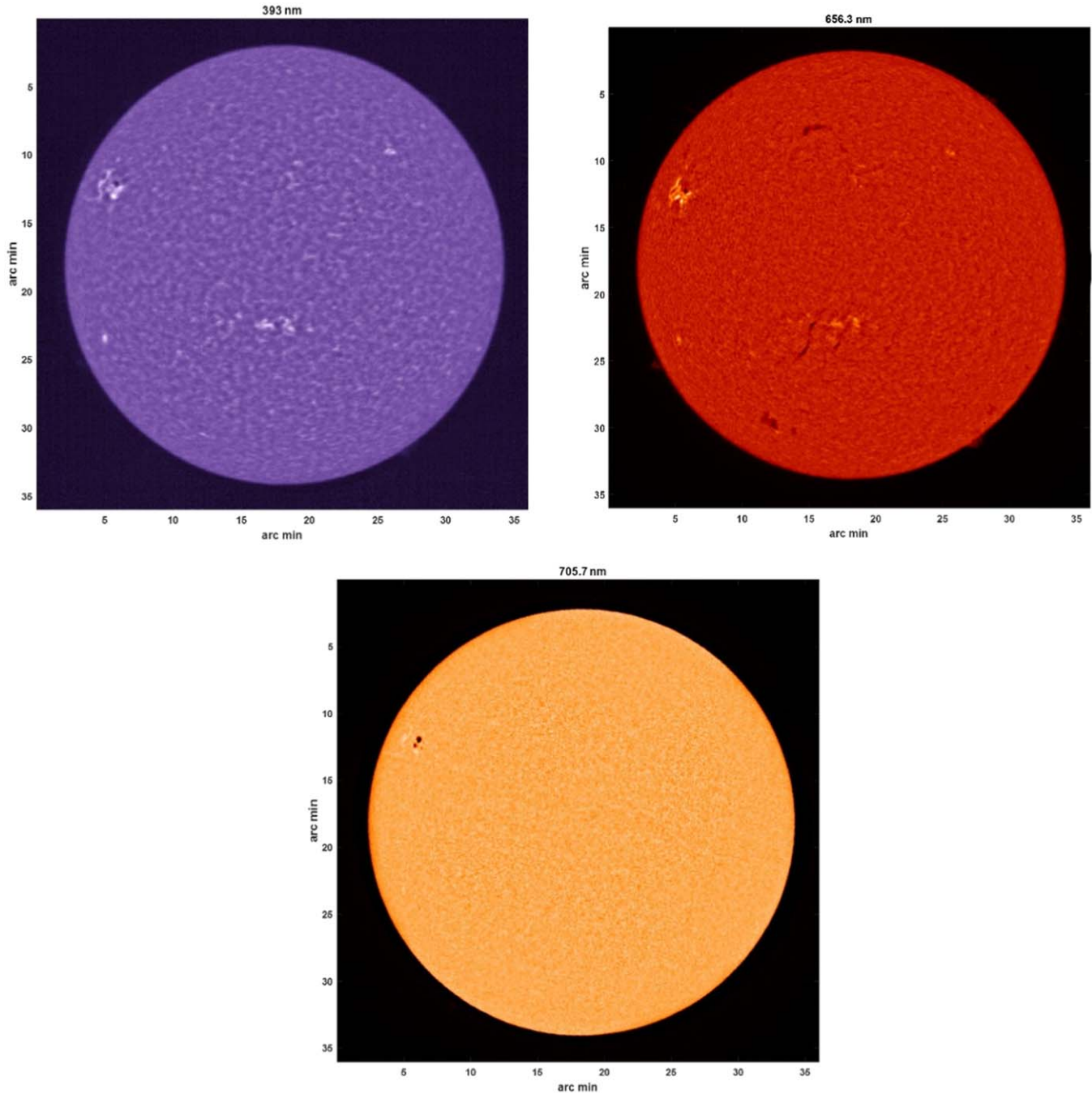


Figure 16. The observations of the three band full disk channels.

according to the theory of Noll (Noll 1976). Figure 10 displays a comparison of open loop and closed loop Zernike mode rms error as well as the Kolmogorov turbulence fitting result. Obviously, the modes from 3rd to 77th are all effectively compensated.

Figure 11 shows the histogram of the Fried parameter r_0 at the time (UT) between 2:47 and 3:03 on 2021 October 3. At

different times, r_0 is always between 3 and 9 cm at the 500 nm wavelength, and its average is about 6 cm. As the AO system kept operating in closed loop during this period, it indicates that this AO system can still work even when $r_0(500\text{ nm})$ is as small as 3 cm.

The fine tracking loop stays closed so as to correct the global tilt and stabilize the image motion. The tracking error

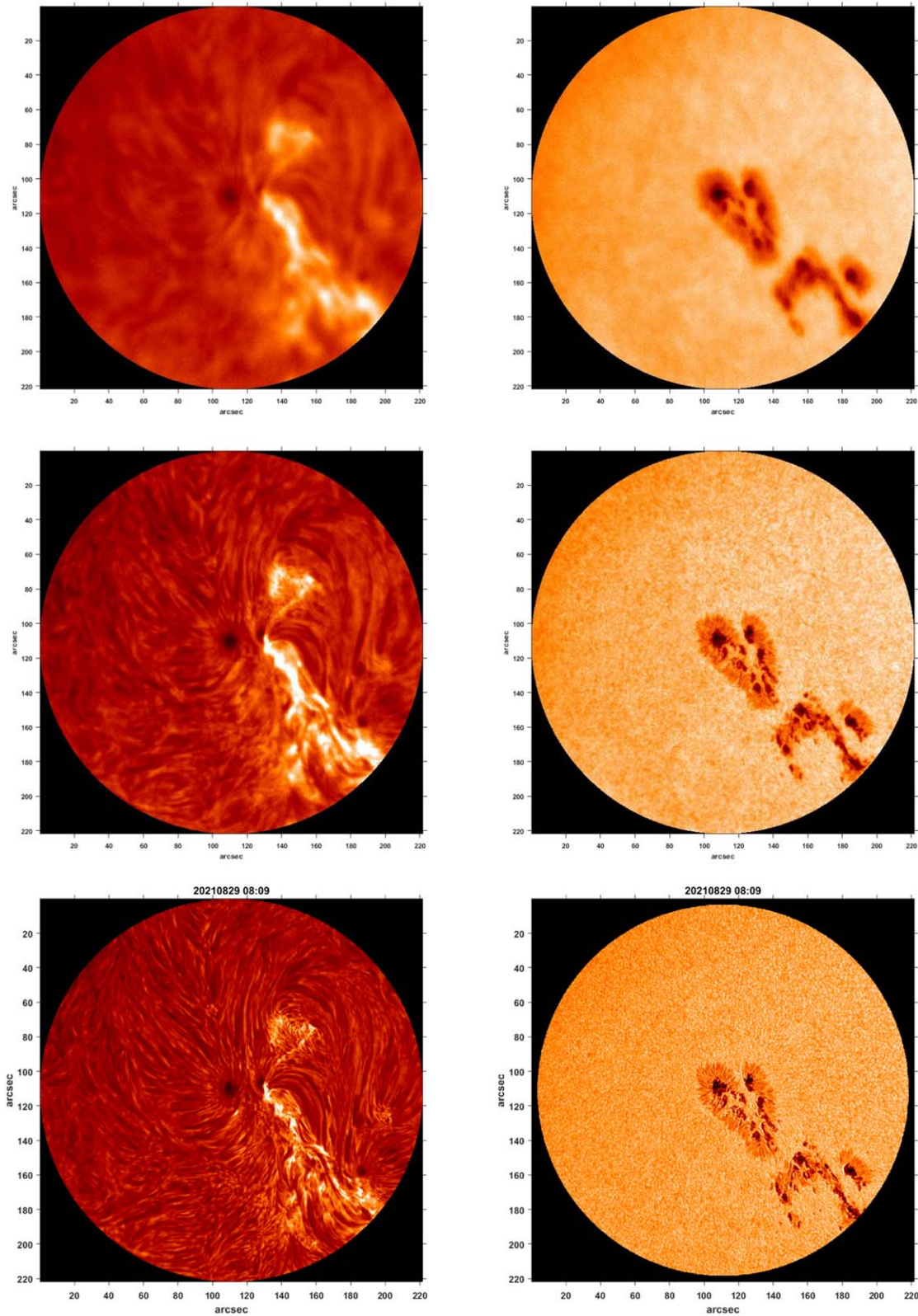


Figure 17. The images of the three observation modes at two high resolution imaging channels ($H\alpha$ band (left), Tio band (right)). The first row is the open loop images, the second row is the AO corrected images and the third row is the speckle reconstruction of the AO images.

distribution is displayed in Figure 12. In most of the cases, the tracking error is below $0''.1$ with an average of $0''.08$.

In this AO system, besides tip-tilt, the remaining 75 higher-order Zernike modes are compensated by the DM. The distribution of high-order closed-loop wavefront errors is depicted in Figure 13, where most of the them are between 20 and 50 nm with an average of 33 nm.

We show an unsharp masked and intensity-clipped image of solar penumbra fibers in Figure 14. Remarkably, these fibers can be distinguished. The intensity cut through the fibers from the lower left to the upper right red line in the image reveals that the width of the central dark lane in the faint fibers is only 3 pixels, that is, $0''.3411$. The interpolated pixels have a distance of $0''.1137$. The red bar in the image plot marks the width of the dark lane between the penumbra fibers. The diffraction limit of the system is $0''.24$. This shows that the system resolution is superior to 1.4 times the diffraction limit.

4. Observation Results

The imaging system of the EAST contains three full disk solar imaging systems at Ca K, $H\alpha$ and TiO bands and two high resolution imaging channels at the $H\alpha$ and TiO bands which are installed on the tube of the main telescope and the Coudé room for solar observation respectively. The parameters of the imaging systems are listed in Table 3.

The full disk photosphere layer (TiO) imaging subsystem is composed of a filter and two groups of spherical lenses. The field of view (FoV) is $66'$ to keep the whole solar image in the FoV.

The layout of the full disk chromosphere ($H\alpha$ and Ca K) imaging optical system is illustrated in Figure 15. The telescope is composed of a transmission Keplerian telescope and imaging lens. Two plane scanning mirrors are placed between the primary and secondary mirrors of the Keplerian telescope to keep the whole solar image in the FoV when the main solar telescope observes the solar active region in the arbitrary position. For narrow band imaging, a Lyot filter is placed in the system.

For the AO-corrected high resolution imaging, in order to prevent vignetting from affecting the imaging quality, the imaging pupil of the system is placed in the middle of the Lyot filter. Therefore, it is necessary to add a beam shrinking component at the rear end of AO as illustrated in Figure 15. The beam shrinking assembly is composed of two groups of achromatic doublets.

The full disk observation channels provide the real time images of the Ca line, $H\alpha$ band and TiO band images, as displayed in Figure 16. The processing procedure of full disk observations contains the flat-fielding, removing the radial profile, removing the large-scale distortion patterns, etc. The

results observed at 10:31 AM on 2021 May 9 are shown at below.

Figure 17 features the imaging observation results from the two high resolution observation channels without AO correction, with AO correction and with speckle reconstruction based on the AO correction (Zhong et al. 2014). The correction of the AO system removes the static aberration and some low-order aberrations of the system, which can significantly improve the imaging quality and signal-to-noise ratio, but it cannot get the effect close to the diffraction limit in a large FoV, so post image reconstruction technology is needed. Speckle image reconstruction technology realizes the high-resolution reconstruction of the target in the frequency domain through the statistical analysis of multiple short exposure images. These results were observed at 8:09 AM on 2021 August 29 of NOAA 12860. From these figures, you can find different features at different heights of the solar atmosphere with high spatial resolution.

5. Summary and Remarks

The EAST was put into operation for the popularization of science in August 2021. Due to the excellent performance of the solar telescope and advanced solar AO system, EAST can also be used for science observations related to solar physics research and space weather prediction.

We would like to express our gratitude to everyone in the EAST team for their efforts. Prof. Wenhan Jiang from IOE, CAS and Prof. Cheng Fang from Nanjing University are also acknowledged for their good suggestions and special support. This work was supported by the National Natural Science Foundation of China (NSFC, Grant Nos. 11727805, 11703029, 11733005 and 12103057).

References

- Cao, W., Gorceix, N., Coulter, R., Coulter, A., & Goode, P. 2010, *Proc. SPIE*, 7733
- Collados, M., Bettonvil, F., Cavaller, L., et al. 2013, *Mem. Soc. Astron.*, 84, 379
- Fang, C., Gu, B., Yuan, X., et al. 2019, *SSPMA*, 49, 059603
- Kisskinova, N., Stoev, A., & Stoev, P. 2011, *BlgAJ*, 17, 10
- Kong, L., Zhang, L., Zhu, L., et al. 2016, *ChOpL*, 14, 100102
- Leslie, S., & Margolis, E. 2017, *Early Popular Visual Culture*, 15, 227
- Liu, Y., Gu, N., & Rao, C. 2015, *OExpr*, 23, 19980
- Liu, Z., Xu, J., Gu, B.-Z., et al. 2014, *RAA*, 14, 705
- Noll, R. J. 1976, *JOSA*, 66, 207
- Rao, C., Gu, N., Rao, X., et al. 2020, *SCPMA*, 63, 109631
- Rao, C., Gu, N., Zhu, L., et al. 2015, *JATIS*, 1, 024001
- Rao, C., Zhang, L., Kong, L., et al. 2018, *SCPMA*, 61, 89621
- Rao, C., Zhu, L., Rao, X., et al. 2010, *ApOpt*, 49, G129
- Rao, C., Zhu, L., Rao, X., et al. 2016a, *ApJ*, 833, 210
- Rao, C., Zhu, L., Rao, X.-J., et al. 2016b, *RAA*, 16, 003
- Rao, C.-H., Jiang, W.-H., Fang, C., et al. 2003, *ChJAA*, 3, 576
- Rimmele, T., Warner, M., Keil, S., et al. 2020, *SoPh*, 295, 172
- Zhong, L., Tian, Y., & Rao, C. 2014, *OExpr*, 22, 29249